The Ninth International Symposium on Linear Drives for Industry Applications

Proceedings

Organized by:

Zhejiang University

Co-organized by:

Linear Motor Institute, Chinese Electrotechnical Society

Institute of Electrical Engineering, Chinese Academy of Science

Technical Co-sponsor:

IEEE Industry Applications Society

Supporters:

National Natural Science Foundation of China

Henful

Parametric design of a linear induction machine for a small scale magnetically levitated train.

G.Glehn, R. Appunn and K. Hameyer
Institute of Electrical Machines, RWTH Aachen University, Germany

***Abstract*—A linear induction machine (LIM) for a small scale magnetically levitated train offers challenges related to the design. An approach is to adapt the design with the help of flux and force analysis on the basis of a parametric finite element (FE) model. Common simulation procedures are compared to each other in relation to their accuracy and complexity. The simulations are validated by measurements of a built prototype.**

***Index Terms*— Linear Induction Machine, Parametric Finite Element Design**

I. Introduction

At the Institute of Electrical Machines of the RWTH Aachen University a small scale magnetically levitated train is developed as a demonstrator of a mechatronic system [1]. The traction drive is a short stator linear induction machine which is designed by analysing the stationary force versus speed characteristic, which is extracted from electromagnetic field simulation obtained by finite element simulations of a parametric machine model. The calculations allow extracting concentrated parameters of the machine's equivalent circuit. The following sections describe the modelling process, the simulation procedures during the design stages and the operation of the prototype.

II. Parametric Geometry

In this section the construction requirements of the maglev train and the chosen geometry parameters of the linear induction machine are introduced.

The linear induction machine consists of a short slotted primary which bears the three phase field winding and a long plane secondary which bears a short-circuiting copper plate. The rail serves as the iron yoke of the secondary. [2] deals with the influence of a plane or slotted design of the secondary. It turned out that a plane design offers almost the same amount of thrust and needs only a fraction of the normal force, which works against the levitation. The short-circuiting copper plate design increases the effective electromagnetic air gap and needs additional magnetization current. The excitation windings in the primary are fed by a symmetric three-phase system. The core of the primary is composed of laminated magnetic sheet steel. To achieve a design which is cheap and simple to construct the phases are not chorded or distributed over slots.

Fig. 1 shows the longitudinal section and the top view.

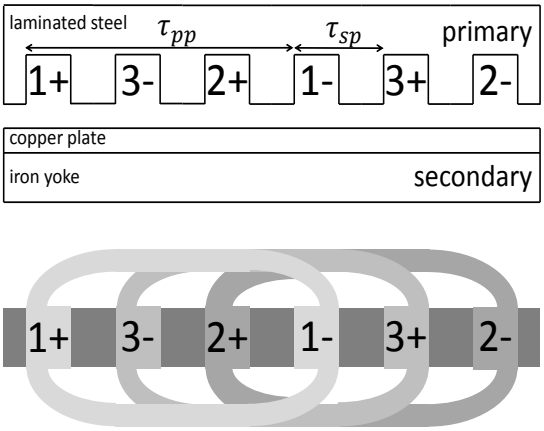

Fig. 1. Three-phase induction motor longitudinal section and top view.

The main machine dimensions are derived from an analytical rough draft which is based on rotating machines. Therefore the thrust is determined in analogy with the tangential force of rotating machines, (1).

$$F = \int \underbrace{\vec{J}}_{\vec{\nabla}\times\vec{H}} \times \vec{B} dV \Rightarrow F = \int H_t \cdot B_n dA \tag{1}$$

The stress tensor (2) which represents the ratio of thrust to the air gap surface is a common design criterion for induction machines. Table I provides the applied values.

$$\sigma = \frac{F}{A} = \frac{1}{\sqrt{2}} \xi_1 H_t B_n \eta \cos\varphi \tag{1}$$

TABLE I
Applied values for analytic dimensioning

ampere conductors per unit length	H_t=30.000 (A/m)
air gap flux density	B=0.5 (T)
efficiency	η=0.5
power factor	cosφ=0.5
winding factor	ξ_1=0.95
thrust	F=20 (N)
force of attraction	< 200 (N)

The result of which is that the air gap surface is determined. The pole pitch ensues from excitation frequency and synchronous speed. The total width is a multiple of the pole pitch. The depth is the quotient of the area and the total width. Nevertheless the dimensions of a slot pitch are still arbitrary. Fig. 2 shows the applied parameters over one slot pitch.

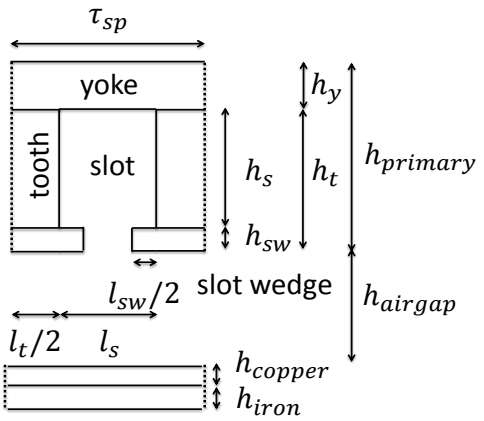

Fig. 2. Applied parameters over one slot pitch.

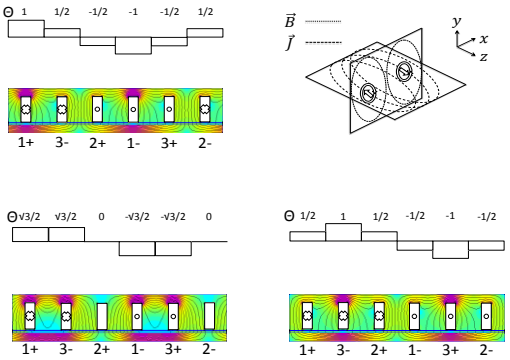

Fig. 3. Travelling magnetic field over one pole pair.

III. Functional Principle

The functional principle of a linear induction machine is based upon the interdependency of two travelling magnetic fields, which move with a certain slip. The slip *s* is defined as the ratio of secondary and primary frequency (*f*), (3).

$$s = frequency_{secondary} / frequency_{primary} \tag{3}$$

The considered fields comply with the frequency condition in (4)

$$frequency_{mechanical} = f_{primary} + f_{secondary} \tag{4}$$

The mechanical frequency $frequency_{mechanical}$ is related with the translation velocity $v_{mechanical}$ (5).

$$frequency_{mechanical} = \frac{v_{mechanical}}{2\tau_{pp}} \tag{5}$$

During one electrical period the travelling magnetic field moves over one pole pair.

The geometry, the excitation and the boundary conditions of the considered machine are constant in the transverse axis (z-axis). In this way the electromagnetic field problem can be solved only in the longitudinal section (xy-plane).

The excitation currents are applied in the z-direction. When using the magnetic vector potential A ($\vec{\nabla}\cdot\vec{A}=0 \quad \vec{\nabla}\times\vec{A}=\vec{B}$), it points in the same direction as the excitation current density J. The curl of the magnetic vector potential in Cartesian coordinates confirms that the magnetic flux density is two dimensional, as in (6).

$$\vec{\nabla}\times\vec{A}(0,0,z)=\begin{pmatrix}\frac{\partial\vec{A}_z}{\partial y} & -\frac{\partial\vec{A}_z}{\partial x} & 0\end{pmatrix}=\vec{B}(x,y,0) \tag{6}$$

Fig. 3 shows the right-angled current density and magnetic flux density in addition to the solution of the travelling magnetic field of a periodic part model of one pole pair at synchronous speed.

The travelling magnetic field is not continuous; it is bound to the dimensions of the primary. Therefore end effects have to be considered, [3]. Fig. 4 shows the end effects for the longitudinal and transversal axis. The longitudinal end effect describes a distortion of the magnetic flux density in the longitudinal direction, which is evoked by the subsiding motional eddy currents in the secondary. The longitudinal end effect is simulated by a model without bounds in the longitudinal direction. The transversal end effect describes a distortion of the magnetic flux density in the transversal direction, which is evoked by a current concentration to the transversal edges of the secondary depending on the proportions of primary and secondary. The transversal end effect is simulated by a model without bounds in the transversal direction. No bounds are applied when enough surrounding air is considered, so that no flux passes out of the model and Dirichlet boundary conditions are permissible at the surrounding air.

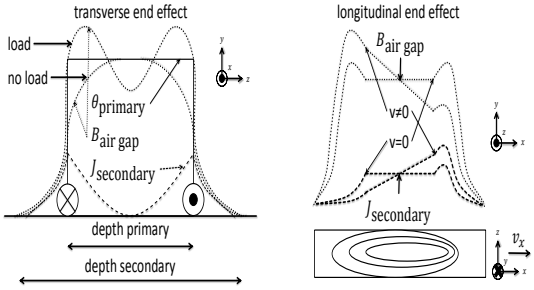

Fig. 4. Linear machines end effects.

IV. Simulation Methods

The force of a linear induction motor is related to eddy currents depending on time and motion. A common approach for representing these eddy currents is to use a transient finite element model, which include the necessary flux variations in Faraday's law. Another common approach is to use a time harmonic model combined with an Euler-term or a slip-transformation, which takes the relative motion between primary and secondary into account. In the following the applied finite

element methods are introduced including the adaptions for the considered problem, [4], [5].

The electromagnetic fields distribution inside an electrical machine corresponds to a magneto quasi static problem in which the displacement current density can be neglected. The strong partial differential equation for the magnetic vector potential is derived from the MAXWELL equations, (7).

$$\vec{\nabla}\times\underbrace{\left(\underbrace{\nu\vec{\nabla}\times\vec{A}}_{\vec{B}}\right)}_{\vec{H}}=\underbrace{\sigma\left(\overbrace{-\vec{\nabla}\phi}^{static}\overbrace{-\frac{\partial\vec{A}}{\partial t}}^{dynamic}\right)}_{\vec{E}}\qquad(7)$$

The solution of the dynamic term is required to receive the correct field distribution including time and motional eddy currents. Due to the transient simulation the complete harmonic spectrum is covered in the solution, so that slot effects and initial responses are visualized. A weighted differential quotient serves for the transient solution of the time derivative of a function *f*(*t*), (8).

$$f(t)=\theta f(t_{n+1})+(1-\theta)f(t_n)$$
$$0\le\theta=\frac{t-t_n}{t_{n+1}-t_n}\le 1\qquad(8)$$

In the time harmonic simulation only one harmonic out of the frequency spectrum is considered. The excitation function becomes a complex rotating phasor. The time derivative is replaced with the product of the imaginary number and the angular velocity of the phasor. A time harmonic simulation with d/d*t*=jω corresponds with the short-circuit point. A static simulation with d/d*t*=0 corresponds with the no load operation of the induction machine, where no eddy currents appear.

Either the motion is taken into account directly (Lagrange) or indirectly (Euler). The direct approach maintains the partial differential equation for every region in a static coordinate system but requires mesh adaption between moving regions, [6]. The indirect approach keeps the mesh and records all regions in the same static coordinate system which requires adaption of the partial differential equation. This assumption is only valid for concurrent surfaces. The field parts caused by motion are represented with an additional term in the electric field strength (9) [7], which cause numerical instability.

$$\underbrace{\overbrace{-\vec{\nabla}\phi}^{static}\overbrace{-\frac{\partial\vec{A}}{\partial t}}^{dynamic\ rest}\overbrace{-\vec{v}\times\left(\vec{\nabla}\times\vec{A}\right)}^{dynamic\ motion}}_{\vec{E}}\qquad(9)$$

Here slip transformation was chosen as preferred method. The stationary force versus speed characteristic is gathered by time harmonic short-circuit simulations under the assumption of constant primary flux linkage. The excitation current is kept constant and the excitation frequency is varied, which matches the variation of the secondary short-circuit resistance. Fig. 5 explains the process.

According to the observed region the forces in the axis of coordination follows with different methods. In all regions the force can be extracted with the Maxwell stress tensor, [8]. The thrust can be calculated with the Lorentz Force inside the eddy current regions or the resistive losses.

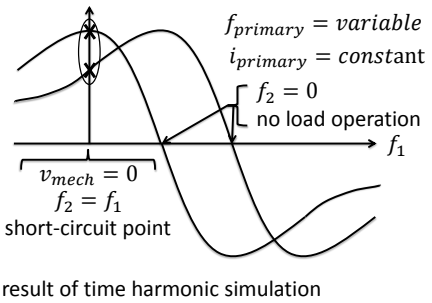

x result of time harmonic simulation

Fig. 5. Constant stator flux force control

V. Parametric Design Process

The parametric design approach makes use of the simplified single phase equivalent circuit diagram of an induction machine which is shown in Fig. 6. The secondary leakage inductance is neglected, because of the homogeneous secondary surface. Out of it the mechanical Power (10) and Force (11) are extracted. It is assumed that the mechanical power is a part of the secondary resistive losses.

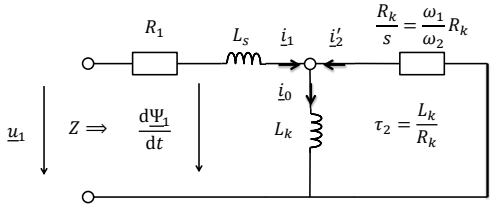

Fig. 6. Single phase equivalent circuit diagram of induction machine.

$$P=m\underline{i}_2^2R_2\left(\underbrace{\frac{1-s}{s}}_{mechanical}+\underbrace{1}_{ohmic}\right)\qquad(10)$$

$$F_{mech}=P_{mech}/v_{mech}$$
$$=3R_2\left|\underline{i}_1\right|^2\frac{1}{\omega_2}\frac{\pi}{\tau_{pp}}\frac{(\omega_2\tau_2)^2}{1+(\omega_2\tau_2)^2}\qquad(11)$$

The slip transformation is utilized to simulate the complete force versus speed characteristic. Two dimensional linear finite element models are used to examine the influence of the geometry parameters on the force. The parameters which are chosen in agreement with the analytically received main dimensions are shown in table II.

TABLE II
APPLIED VALUES FOR PARAMETER SET

Height iron	[10]mm
Height slot wedge	[10]mm
Height slot	[10]mm
Height tooth	Height slot wedge + Height slot
Height air gap	[1] mm
Height yoke	[10]mm
Length yoke	< 500 mm
Depth	[30] mm
Height copper sheet	[0 1 **2** 3] mm
Length tooth	[5 **10** 15 20 30 40] mm
Length slot	[10 15 20 25 **30** 40]mm
Length slot wedge	[**0** 1/3 1/2 2/3] l_s

The following diagrams show the influence of the variation of one of the parameters when the others are maintained. The comparability of the charts is difficult, because the machine geometry changes and therefore the slip is not determined directly. The values for the maintained parameters are typed in bolt in Table I.

First the thickness of the copper plate is varied; Fig. 7. Because of the lower electrical conductivity the iron rail has a higher pull out slip frequency which is not desired here. The more the copper plate is thick, the more the forces drop, since the magnetic leakage flux is higher.

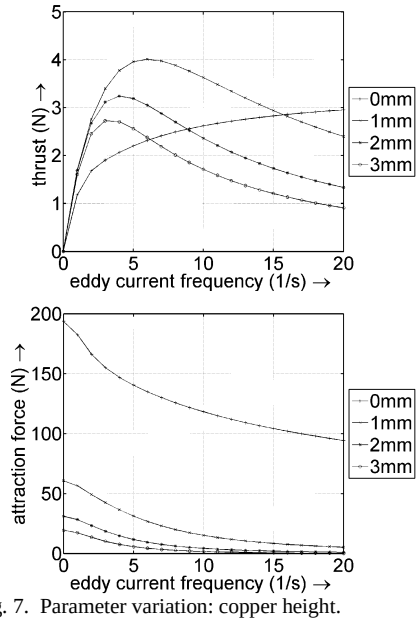

Fig. 7. Parameter variation: copper height.

Next the tooth length is varied; Fig. 8. The more the tooth length growth, the more the pull out slip frequency drops. The magnetizing inductance increases with the tooth size. The smallest possible slip is desirable.

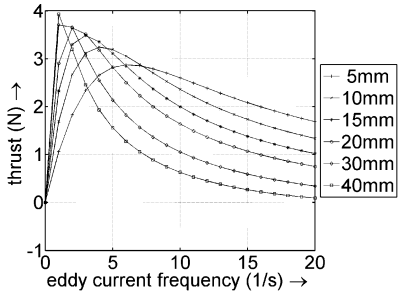

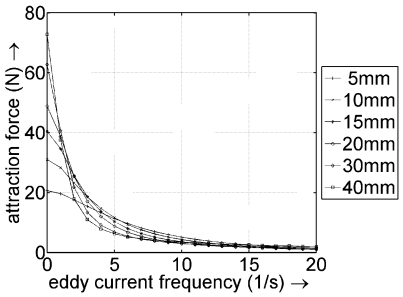

Fig. 8. Parameter variation: tooth length.

Here after the slot length is varied; Fig.9. The current linkage changes, because the current density inside the slots is kept constant. The force reveals a quadratic dependence on the current linkage.

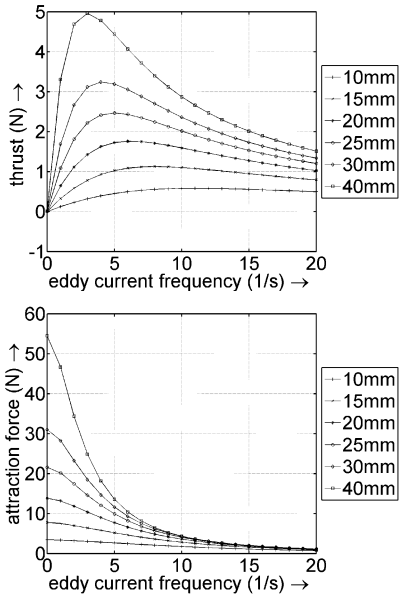

Fig. 9. Parameter variation: sloth length.

Finally the sloth wedge is varied; Fig. 10. Closed slots attain higher forces. The resistance seen by the eddy currents is smaller for closed slots, because they encircle smaller paths.

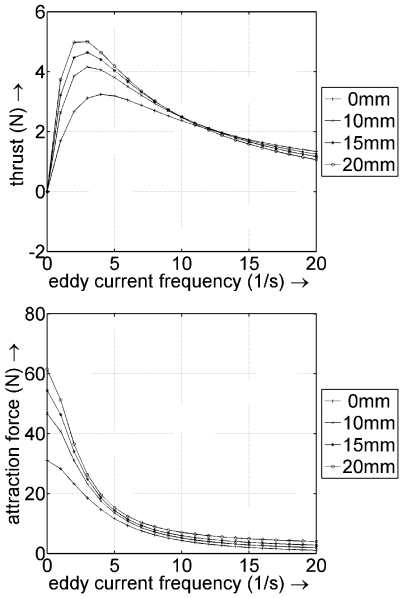

Fig. 10. parameter variation: slot wedge.

Fig. 11 shows on the left side the design archived by simulations and on the right side an equivalent design. The equivalent design is built up, because of its simpler manufacture of the end turns, although it demands more magnetic sheet steel.

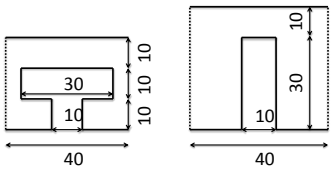

Fig. 11. archived designs.

The equivalent circuit parameters are extracted from the force (11) or flux-linkage (12) [9], [10].

$$u_1 = i_1 \underline{Z} = R_1 i_1 + \frac{d}{dt}\Psi_1$$
$$= R_1 i_1 + \underbrace{j\omega_1}_{\frac{d}{dt}} \underbrace{\left(L_s + L_k \frac{1}{1 + j\omega_2 \tau_2} \right) i_1}_{\Psi_1 = Li} \qquad (12)$$

Fig. 12 shows the simulated values as crosses and the fitted values as lines. The extracted equivalent circuit parameters are: R_1=1Ω; L_s=49,7mH; L_k=238,6mH; R_k=5,39Ω.

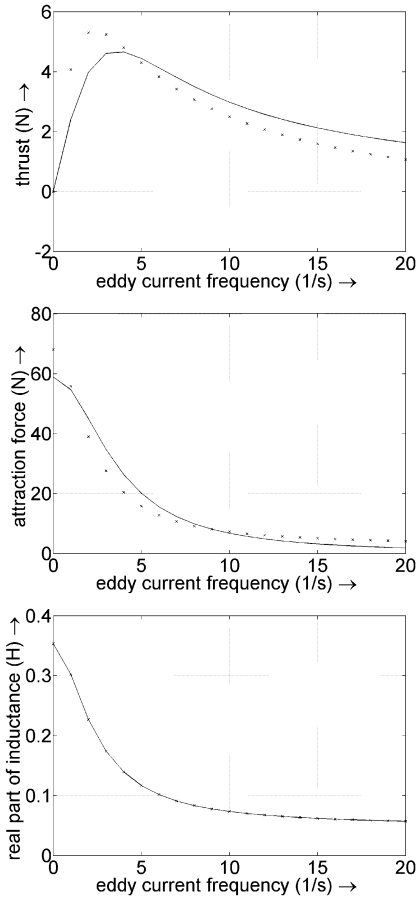

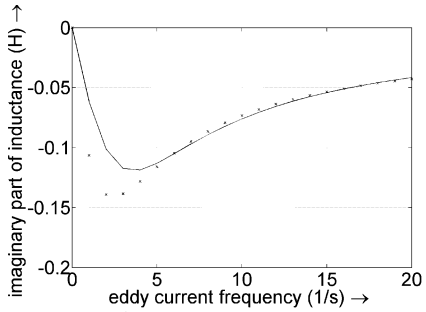

Fig. 12. Fitting of equivalent circuit parameters.

VI. Comparison of Measurement and Simulation

A prototype of the linear induction motor is built into the introduced maglev train, Fig 12. The force versus speed characteristic is measured for constant primary flux linkage (open loop control I/f) and compared to simulation results, Fig 13.

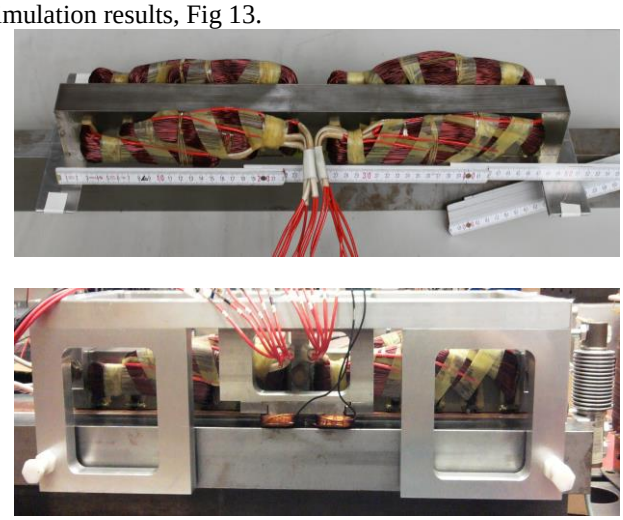

Fig. 12. Linear induction machine built into maglev train.

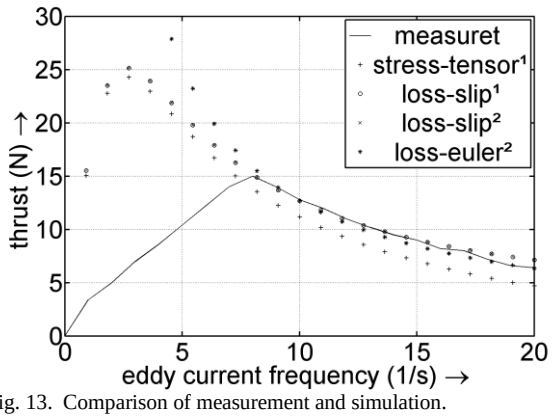

Fig. 13. Comparison of measurement and simulation.

It turns out that the force which is calculated on the power loss is slightly greater than for Maxwell stress tensor. The force calculated with addition of an Euler term is not able to portray the pull out slip frequency, because it has no inflection point. The measured curve shows significant deviations from the simulation, which therefore appears to have wrong material parameters. The simulations marked with ¹ are done with FEMM and the simulations marked with ² are done in Octave.

So far the influence of the longitudinal end effect is not mentioned. Fig 14 sows the comparison between the simulated forces of a nonlinear transient full model of one pole pair. The longitudinal end effect reduces the thrust significantly and increases the pull out slip frequency.

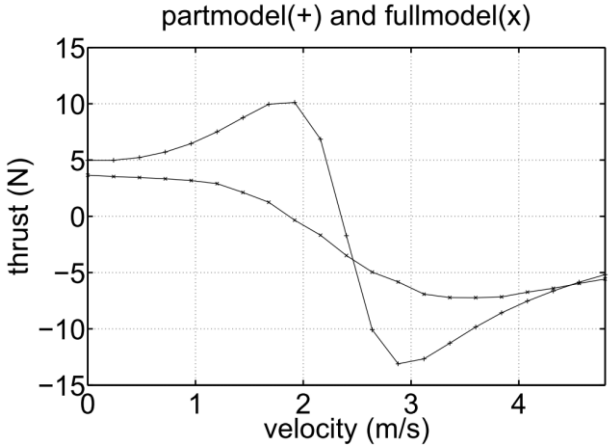

Fig. 14. comparison of nonlinear transient 2D simulations.

The prediction of the simulations, that the force is not central symmetric and the synchronous speed is shifted demands further investigations.
So far the influence of the transverse edge effect is not mentioned. [11] deals with the simulations of a transient 3D finite element model, which is necessary to portray the transverse edge effect. [12] shows the comparison between 2D and 3D simulations of a linear eddy current brake, whose machine characteristic corresponds with the one of a linear induction motor., with concentrated winding and zero primary frequency. It turned out, that the simulated force of a 3D model is significantly lower than the simulated force of a 2D model. The reason for the higher eddy currents in the 2d simulation is a neglecting of resistance, because of missing eddy currents bounds. Therefore it is admirable to simulate a 3D model to archive a desirable accuracy.

VII. Conclusions

This paper describes characteristic analysis of single-sided linear induction machine with short primary and flat secondary according to the parameters of the geometry. The change of the equivalent circuit parameters according to the primary conductor shape is comprehended by 2D finite element simulations. The simulations are confirmed by measurements of a built up prototype. The results of the applied approaches promise a quick view of the stationary machine characteristic. The accuracy of the introduced approaches dependents on the applied simplifications. In particular, the material properties and linear end effect require adjustments to the simulations methods.

References

[1] R. Appunn, T. Herold und K. Hameyer, „Development of a small scale magnetically levitated train as demonstrator for undergraduate mechatronics students," in *Optimization of Electrical and Electronic Equipment (OPTIM), 2012 13th International Conference on*, 2012.

[2] B.-J. Lee, D.-H. Koo und Y.-H. Cho, „Investigation of Linear Induction Motor According to Secondary Conductor Structure," *#IEEE_J_MAG#*, Bd. 45, Nr. 6, pp. 2839-2842, 2009.

[3] J. Lu und W. Ma, „Research on End Effect of Linear Induction Machine for High-Speed Industrial Transportation," *Plasma Science, IEEE Transactions on*, Bd. 39, Nr. 1, pp. 116-120, 2011.

[4] M. Mirsalim, A. Doroudi und J. S. Moghani, „Obtaining the operating characteristics of linear induction motors: a new approach," *#IEEE_J_MAG#*, Bd. 38, Nr. 2, pp. 1365-1370, 2002.

[5] S.-M. Jang, Y.-S. Park, S.-Y. Sung, K.-B. Lee, H.-W. Cho und D.-J. You, „Dynamic Characteristics of a Linear Induction Motor for Predicting Operating Performance of Magnetic Levitation Vehicles Based on Electromagnetic Field Theory," *#IEEE_J_MAG#*, Bd. 47, Nr. 10, pp. 3673-3676, 2011.

[6] E. Lange, F. Henrotte und K. Hameyer, „A Variational Formulation for Nonconforming Sliding Interfaces in Finite Element Analysis of Electric Machines," *#IEEE_J_MAG#*, Bd. 46, Nr. 8, pp. 2755-2758, 2010.

[7] D.-H. Im und C.-E. Kim, „Finite element force calculation of a linear induction motor taking account of the movement," *Magnetics, IEEE Transactions on*, Bd. 30, Nr. 5, pp. 3495-3498, 1994.

[8] F. Henrotte und K. Hameyer, „A Theory for Electromagnetic Force Formulas in Continuous Media," *#IEEE_J_MAG#*, Bd. 43, Nr. 4, pp. 1445-1448, 2007.

[9] E. B. S. Filho, A. M. N. Lima und C. B. Jacobina, „Parameter estimation for induction machines via non-linear least squares method," in *Proc. IECON '91. Conf. Int Industrial Electronics, Control and Instrumentation*, 1991.

[10] D. Dolinar, G. Stumberger und B. Grcar, „Calculation of the linear induction motor model parameters using finite elements," *#IEEE_J_MAG#*, Bd. 34, Nr. 5, pp. 3640-3643, 1998.

[11] D. Albertz, S. Dappen und G. Henneberger, „Calculation of the 3D nonlinear eddy current field in moving conductors and its application to braking systems," *Magnetics, IEEE Transactions on*, Bd. 32, Nr. 3, pp. 768-771, 1996.

[12] M. Hofmann, T. Werle, R. Pfeiffer und A. Binder, „2D and 3D numerical field computation of eddy-current brakes for traction," *Magnetics, IEEE Transactions on*, Bd. 36, Nr. 4, pp. 1758-1763, 2000.